



# Methane abatement under stoichiometric conditions on perovskite-supported palladium catalysts prepared by flame spray synthesis



Ye Lu<sup>a</sup>, Katarzyna A. Michalow<sup>b,d</sup>, Santhosh Kumar Matam<sup>a</sup>, Alexander Winkler<sup>c,1</sup>, Alexandra E. Maegli<sup>a</sup>, Songhak Yoon<sup>a</sup>, Andre Heel<sup>e</sup>, Anke Weidenkaff<sup>a</sup>, Davide Ferri<sup>d,\*</sup>

<sup>a</sup> Empa, Swiss Federal Laboratories for Materials Science and Technology, Laboratory for Solid State Chemistry and Catalysis, Ueberlandstrasse 129, CH-8600 Dübendorf, Switzerland

<sup>b</sup> Empa, Swiss Federal Laboratories for Materials Science and Technology, Laboratory for High Performance Ceramics, Ueberlandstrasse 129, CH-8600 Dübendorf, Switzerland

<sup>c</sup> Empa, Swiss Federal Laboratories for Materials Science and Technology, Internal Combustion Engines Laboratory, Ueberlandstrasse 129, CH-8600 Dübendorf, Switzerland

<sup>d</sup> Paul Scherrer Institut, CH-5232 Villigen PSI, Switzerland

<sup>e</sup> ZHAW, School of Engineering, Institute of Materials and Process Engineering, Technikumstrasse 9, CH-8400 Winterthur, Switzerland

## ARTICLE INFO

### Article history:

Received 26 July 2013

Accepted 1 August 2013

Available online 11 August 2013

### Keywords:

Perovskite-type oxides

Palladium

Flame spray synthesis (FSS)

Methane oxidation

Stoichiometric conditions

## ABSTRACT

Three-way catalysts (TWC) are the key technology to reduce emissions of pollutants from stoichiometric engines. Perovskite-type catalysts of general formula  $ABO_{3\pm\delta}$  ( $A = La, Y$ ;  $B = Mn, Fe$ ) containing 2 wt% Pd were produced by flame spray synthesis (FSS) using metal nitrate precursors. The structural properties of the catalysts were characterized by X-ray diffraction (XRD), surface area determination (BET) and transmission electron microscopy (TEM). Crystalline metal oxide nano-particles of 20 nm average size were accompanied by minority  $La_2O_3$  and  $Y_2O_3$  phases. The state of Pd in the catalysts was characterized using X-ray photoelectron spectroscopy (XPS), X-ray absorption near edge spectroscopy (XANES) and CO adsorption by infrared spectroscopy. Metallic Pd coexisted with Pd in oxidation state +2 and higher on all fresh samples. TEM confirmed the presence of dispersed Pd particles 2–5 nm in diameter. Therefore, under the chosen synthesis conditions, FSS provides supported palladium nano-particles rather than a solid solution. PdO was the dominant Pd species after calcination at 700 °C. The TWC activity was tested in a simulated stoichiometric gas mixture comprising  $CH_4$ , CO,  $NO_x$  and  $O_2$ . PdO in combination with  $YFeO_{3\pm\delta}$  exhibited the lowest temperature for  $CH_4$  oxidation ( $T_{50} = 450$  °C), which was ca. 100 °C lower than that of the sample obtained by the conventional wet-chemical method. After cycling under reaction conditions up to 850 °C, a large improvement of catalytic activity for  $CH_4$  oxidation was observed which associated with the formation of metallic Pd particles (ca. 20 nm) and the hexagonal → orthorhombic phase transition of  $YFeO_{3\pm\delta}$ .

© 2013 Elsevier B.V. All rights reserved.

## 1. Introduction

Natural gas and biogas are attractive alternative fuels to gasoline and diesel for motor vehicles. This calls for material design of suitable catalytic converters for pollution control in order to comply with the stringent emission regulations. Current aftertreatment technologies for stoichiometric engines fuelled by compressed natural gas (CNG) are based on palladium containing three-way catalysts (TWC) that are most efficient at stoichiometric

air-to-fuel ratio ( $\lambda = 1$ ) [1]. Palladium (Pd) is relatively cheap among the platinum group metals (PGM) and is considered as the most active for total oxidation of methane [2]. Though conventional TWC are very efficient, they suffer from the deactivation caused mainly by sintering of Pd and the metal oxide support as a result of severe redox reaction conditions and high temperature surges within the catalytic converter [3]. Perovskite-type oxides have been indicated as potential components of TWC due to the possibility to stabilize the PGM through its interaction with the perovskite lattice [4,5]. In response to the periodic reducing and oxidizing reaction conditions, Pd seems to be capable to segregate and re-dissolve into the  $ABO_3$  lattice, respectively, thus preventing extensive particle sintering under prolonged operation and at high temperatures. This controversial self-regenerative function [6] has

\* Corresponding author. Tel.: +41 56 310 2781.

E-mail address: [davide.ferri@psi.ch](mailto:davide.ferri@psi.ch) (D. Ferri).

<sup>1</sup> Present address: Hug Engineering AG, Im Geren, CH-8352 Elsau, Switzerland.

**Table 1**  
Physico-chemical properties of the catalysts.

Sample	Entry name	SSA (m <sup>2</sup> /g) Fresh	SSA (m <sup>2</sup> /g) Calc <sup>a</sup>	Pd content <sup>b</sup> wt%	Pd content <sup>b</sup> at%	XRD <sup>c</sup>	OSCC <sup>d</sup> μmol O <sub>2</sub> /g
LaFeO <sub>3±δ</sub>	LFO	28	17	–	–	o + La <sub>2</sub> O <sub>3</sub>	173
LaMnO <sub>3±δ</sub>	LMO	18	17	–	–	o + La <sub>2</sub> O <sub>3</sub>	490
YFeO <sub>3±δ</sub>	YFO	27	19	–	–	h + Y <sub>2</sub> O <sub>3</sub>	416
YMnO <sub>3±δ</sub>	YMO	34	31	–	–	h + Y <sub>2</sub> O <sub>3</sub>	875
La(Fe,Pd)O <sub>3±δ</sub>	LFPO	22	17	1.82 ± 0.03	0.84	o + La <sub>2</sub> O <sub>3</sub>	176
La(Mn,Pd)O <sub>3±δ</sub>	LMPO	32	18	1.79 ± 0.01	0.82	o + La <sub>2</sub> O <sub>3</sub>	597
Y(Fe,Pd)O <sub>3±δ</sub>	YFPO	36	19	1.75 ± 0.02	0.64	h + Y <sub>2</sub> O <sub>3</sub>	504
Y(Mn,Pd)O <sub>3±δ</sub>	YMPO	33	31	1.71 ± 0.01	0.62	h + Y <sub>2</sub> O <sub>3</sub>	961
YFeO <sub>3±δ</sub>	YFO <sub>CM</sub> <sup>e</sup>	–	9	–	–	h	–
Y(Fe,Pd)O <sub>3±δ</sub>	YFPO <sub>CM</sub> <sup>e</sup>	–	12	2.37 ± 0.01	0.86	h	505

<sup>a</sup> Conditions: 700 °C for 2 h, in air.

<sup>b</sup> By ICP-OES.

<sup>c</sup> Fresh samples. o: orthorhombic; h: hexagonal. LMPO undergoes orthorhombic to rhombohedral phase transition upon calcination.

<sup>d</sup> Oxygen storage capacity complete at 400 °C (by TG analysis).

<sup>e</sup> Prepared by the amorphous citric acid method.

been extensively described with respect to gasoline stoichiometric engines, whereas the research is rarely undertaken with natural gas fuel and methane [7]. Tzimpilis et al. [8] reported the TWC activity of La–Mn–O substituted with low amounts of Pd. Catalyst activation was observed, which was ascribed to the segregation of Pd as a result of the high-temperature hydrothermal conditions experienced during operation.

It has been recognized that the activity of especially La-based perovskite-type (ABO<sub>3±δ</sub>) oxidation catalysts is largely governed by their defect chemistry and oxygen diffusion properties [9,10]. However, the nature and size of the A-site rare-earth element play a crucial role to determine the physico-chemical properties of the mixed oxides. Replacement of La<sup>3+</sup> (1.17 Å) by smaller size ions like Y<sup>3+</sup> (1.04 Å) [11] introduces a large structural distortion that can change interatomic distances and microstructural properties. As a result, both oxygen content and mobility and consequently catalytic activity can be strongly affected. A few studies have demonstrated the potential of Y-based perovskite-type catalysts. Orthorhombic YFeO<sub>3</sub> and YMnO<sub>3</sub> exhibit weak ferromagnetic behaviour [12] and possess good photocatalytic properties [13]. Orthorhombic YCo<sub>0.5</sub>Mn<sub>0.5</sub>O<sub>3</sub> exhibited superior catalytic activity for methane oxidation compared to corresponding La and Er based catalysts [14]. Furthermore, the metastable hexagonal structure of YFeO<sub>3</sub> can be easily formed in the presence of Pd, which showed high catalytic activity for CO [15] and CH<sub>4</sub> oxidation [16]. Despite its different crystal structure, which ultimately affects the possible coordination environment of Pd at Fe sites, this material possesses 'self-regenerative' properties [15].

The activity and stability of catalyst nano-particles is strongly dependent on their size, shape, surface structure as well as the bulk and surface composition. These parameters can be tuned by the choice of appropriate synthesis methods. Flame-spray synthesis (FSS) is a well-established single step method to provide high yield of nano-materials using economic precursors [17–23]. Small crystal size and a sufficient thermal resistance against sintering are the key properties of a perovskite catalyst [18], which can be obtained by FSS. Additionally, the potential of FSS to produce novel and metastable phases with unusual properties, which may not be reproducible by conventional wet chemical methods is also known [24]. However, the particle formation mechanism is largely dependent on synthesis parameters and the homogeneity of the particles depends on the selection of the metal precursors [25,26]. FSS is a suitable method to produce perovskite-type oxides for the flameless methane oxidation [17,27–29].

In this work, we use a unique high temperature acetylene flame to produce Pd-substituted perovskite-type oxides from metal nitrate precursors of La and Y as the A-site cations and of Fe and Mn

as the B-site cations and of Pd. The aim is the single step synthesis of potential TWC components for the exhaust aftertreatment of stoichiometric engines fuelled with natural gas. The materials are tested under stoichiometric air-to-fuel ratio and their performance is compared with that of a conventional model TWC.

## 2. Experimental

### 2.1. Catalyst preparation

Perovskite-type oxides of the general composition A(B,Pd)O<sub>3</sub> (A = La or Y; B = Mn or Fe) containing nominally 2 wt% Pd were prepared by flame spray synthesis (FSS). Metal nitrates, La(NO<sub>3</sub>)<sub>3</sub>·6H<sub>2</sub>O (99%, Auer Remy), Mn(NO<sub>3</sub>)<sub>2</sub>·4H<sub>2</sub>O (97%, Fluka), Fe(NO<sub>3</sub>)<sub>3</sub>·6H<sub>2</sub>O (98–101%, Fluka), Y(NO<sub>3</sub>)<sub>3</sub>·6H<sub>2</sub>O (99.9%, ABCR) and Pd(NO<sub>3</sub>)<sub>2</sub> (4.424 wt% Pd solution, Alfa Aesar) were dissolved in a 1:3 mixture of deionized water and *N,N*-dimethylformamide (DMF, 99%, Sigma–Aldrich) [23]. The total metal nitrate concentration was kept constant at 1 mol/l. DMF serves as a fuel with a high boiling point (153 °C) and high combustion enthalpy (−1941.9 kJ/mol), which increases the flame temperature to facilitate the conversion of non-volatile precursors into oxides [23].

The detailed FSS setup has been described elsewhere [21,30]. Briefly, each of the precursor solutions was pumped at 20 ml/min by double syringes through a capillary, atomized by a flow of 35 l/min O<sub>2</sub> and ignited by six circularly arranged acetylene/oxygen flamelets (13/17 l/min), resulting in a ca. 20 cm long flame. The acetylene/oxygen flame exhibits a higher heat capacity (44 kJ/mol) than the commonly used CH<sub>4</sub> flame (36 kJ/mol) thus enabling the decomposition of non-volatile nitrates into oxides and sustaining the presence of water. The nano-powders were collected on glass fiber filters (Whatman GF1) via a vacuum pump. A calcination treatment in air at 700 °C for 2 h was chosen after TGA analysis of the freshly prepared powders (Fig. S1). In the following, the catalysts are labelled as reported in Table 1.

For comparison, the best perovskite-type catalyst in terms of TWC activity was also prepared by the conventional amorphous citric acid method and calcined at 700 °C [16]. The reference conventional powder TWC was composed of Pd, alumina and ceria-zirconia (Pd/ACZ; 1.6 wt% or 0.3 at% Pd; SSA = 135 m<sup>2</sup>/g) and was kindly provided by Umicore.

### 2.2. Characterization

The Pd content of the catalysts was determined by inductively coupled plasma optical emission spectrometry (ICP-OES, Agilent 7500cx) (for details see [31]).

The specific surface area (SSA) was determined by the BET single-point method (QuantaChrom ChemBET 3000) using 30 vol% N<sub>2</sub>/He. Prior to the measurements, all samples were degassed at 200 °C for 30 min in pure N<sub>2</sub>. Temperature programmed reduction by hydrogen (H<sub>2</sub>-TPR) was performed on the same instrument using the same pretreatment procedure. The H<sub>2</sub>-TPR experiments were performed between 25 and 900 °C at 5 °C/min in 5 vol% H<sub>2</sub>/He (20 ml/min). The oxygen storage capacity complete (OSCC) defined as the total amount of desorbed oxygen was determined under static conditions using a thermogravimetric method [32]. The pre-calcined samples were treated with 5% H<sub>2</sub>/Ar at 400 °C for 70 min. The observed weight loss was converted into the corresponding oxygen content assuming that the sample is fully oxidized in its initial state.

The phase purity of fresh and calcined samples was analyzed by X-ray diffraction (X'Pert Pro PANalytical) using monochromatic Cu K $\alpha_1$  radiation ( $\lambda = 1.54056 \text{ \AA}$ ). The diffraction patterns were recorded between 20° and 80° (2 $\theta$ ) with an angular step interval of 0.0167°. Phase identification was performed using the ICDD database in the software X'Pert Highscore Plus (PANalytical). The Rietveld refinement program, *FullProf* [33] was used to determine the quantity of different phases in La-based catalysts. The Thompson-Cox-Hastings pseudo-Voigt function was chosen as profile function [34]. The instrumental contribution for peak broadening was estimated with the measurement of the standard reference sample CeO<sub>2</sub> (NIST SRM674b). The Rietveld refinement for the quantitative phase analysis was not satisfactory for Y-based catalysts mainly due to the strong overlap of the Y<sub>2</sub>O<sub>3</sub> with YFeO<sub>3</sub> phases.

The microstructure and morphology of the powders were observed by electron microscopy. A Jeol 2200FS transmission electron microscope (TEM) equipped with 200 kV field emission gun and an in-column energy filter was used to obtain high spatial resolution images of the sample crystal structure. Additionally, images with atomic number ( $Z^{1.5-1.8}$ ) contrast were provided in the high-angle annular dark field (HAADF) STEM mode [35]. The local composition was determined by energy dispersive X-ray spectroscopy (EDS). The samples were prepared by deposition via an ethanol suspension onto a carbon film coated copper grid (Plano GmbH). The interplanar distance ( $d$ ) was measured by averaging the distances between successive peaks in the contrast profile taken along a line perpendicular to the fringes in the software *DigitalMicrograph* [36].

Diffuse reflectance infrared Fourier transform spectroscopy (DRIFTS) data were collected at a resolution of 4 cm<sup>-1</sup> using a VERTEX 70 FT-IR spectrometer (Bruker Optics) equipped with a high temperature reaction chamber (Praying Mantis, Harrick) and a liquid-nitrogen cooled MCT detector. The cell was connected to a temperature control unit and a gas manifold. Prior to CO adsorption, the samples were exposed to 20 vol% O<sub>2</sub>/Ar (50 ml/min) at 500 °C for 30 min, followed by reduction at 300 °C for 30 min in 10 vol% H<sub>2</sub>/Ar. After changing to Ar flow and cooling to room temperature, a background spectrum was obtained prior to CO adsorption in 5 vol% CO/Ar.

X-ray photoelectron spectroscopy (XPS) measurements were performed on pellets using monochromatic Al K $\alpha$  radiation and a hemispherical capacitor electron-energy analyzer equipped with a channel plate and a position-sensitive detector (PHI Quantum 2000). The electron take-off angle was 45° and the analyzer was operated in the constant pass energy mode for all measurements. The beam diameter was typically 100  $\mu\text{m}$ . All the spectra were corrected for electrical charging by positioning the C1s peak at 284.8 eV. The analyzer pass energy was set to 58.7 eV for the survey spectra (used for quantification) and to 46.95 eV for the detail spectra. The spectra were analyzed with the software *CasaXPS* and the

relative sensitivity factors given by the PHI MultiPak library were used for the quantification.

X-ray absorption near edge spectroscopy (XANES) data of Pd-containing catalysts were recorded in the transmission mode at the Pd  $K$ -edge (24.35 keV) using a Si (311) monochromator at the beamline X1 of Hasylab (DESY, Hamburg). The spectrum of the Pd foil was simultaneously collected for energy calibration. The required sample amount was homogeneously mixed with polyethylene and pressed into pellets. The spectra were energy and background corrected and normalized with the software *Athena* [37].

### 2.3. Three-way catalytic activity

The light-off profiles of the catalysts were obtained in a simulated exhaust mixture comprising 7000 ppm CO, 1300 ppm CH<sub>4</sub>, 1600 ppm NO<sub>x</sub> and 5300 ppm O<sub>2</sub> (He balance; 100 ml/min). The reaction was performed between 25 and 850 °C in a quartz-tube reactor ( $d = 6 \text{ mm}$ ) using catalyst particles (150–200  $\mu\text{m}$ ; 100 mg) diluted with the same volume and sieved fraction of sea sand and firmly fixed in the middle of the reactor between two quartz wool plugs. Prior to reaction, the catalysts were treated in 20 vol% O<sub>2</sub>/He (50 ml/min) at 700 °C for 2 h. The samples were not further treated between consecutive activity runs. The gas hourly space velocity (GHSV) was 60,000 h<sup>-1</sup>. The outlet of the reactor was analyzed with a gas chromatograph (Agilent 3000A Micro GC) equipped with two columns (PoraPLOT-Q for CH<sub>4</sub>, CO<sub>2</sub>, H<sub>2</sub>O, N<sub>2</sub>O; molecular sieve 5  $\text{\AA}$  for CO and NO). The activity data of the catalysts were compared with that of the Pd/ACZ catalyst.

## 3. Results and discussion

### 3.1. Structural properties

The physico-chemical properties of all catalysts are reported in Table 1. All flame-made catalysts exhibit a specific surface area of about 30 m<sup>2</sup>/g, with the exception of LMO and LFPO. The corresponding crystallite size obtained by the Scherrer equation [38] varies between 30 and 50 nm. However, uncombusted metal precursor residues and amorphous phases are present in the as-synthesized materials due to short residence time in the flame and the rapid quenching process during the flame spray synthesis. Therefore, a post-synthesis calcination procedure is applied. The calcination temperature is determined by evaluating the mass loss and evolution of phase composition of the samples in TGA, where all samples behave similarly. Taking LFPO as an example (Fig. S1), all IR observable residual species (Fig. S2) are removed at around 700 °C. It is worth mentioning that the total mass loss of the sample is within 5% up to 1000 °C, thus implying a considerable thermal stability of the flame-made materials. By increasing the calcination temperature to 900 °C, the phase purity of LFO greatly improves (Fig. S3), but the SSA decreases significantly from 28 to 5 m<sup>2</sup>/g. Therefore, the calcination temperature of 700 °C is selected to balance the phase purity and SSA. After calcination, the SSA of the catalysts decreases to an average value of around 17–19 m<sup>2</sup>/g with exception of LMO and YMO. The SSA of YMO and YMPO are least affected by calcination at 700 °C.

The sharp reflections of the XRD patterns of the fresh Pd-containing samples shown in Fig. 1 indicate high degree of crystallinity even before calcination. The low signal to noise ratio of the XRD patterns reveals the nanocrystalline nature of the samples. The Pd-free support oxides exhibit identical XRD patterns (not shown). The perovskite-type ABO<sub>3</sub> is the major phase (77–87 wt%) in all samples. LFPO and LMPO exhibit orthorhombic LaFeO<sub>3</sub> (PDF 01-074-2203) and LaMnO<sub>3</sub> (PDF 01-087-2012) structures

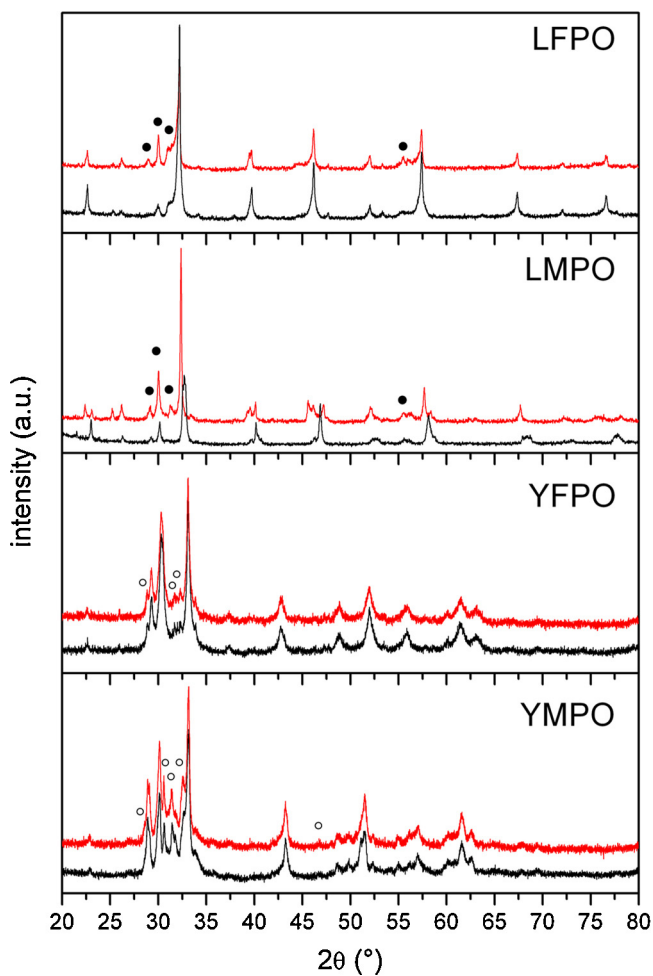


**Fig. 1.** XRD patterns of fresh (red) and calcined (black) Pd-containing perovskite-type oxides. Secondary phases: (●)  $\text{La}_2\text{O}_3$ , (○)  $\text{Y}_2\text{O}_3$ . (For interpretation of the references to color in figure legend, the reader is referred to the web version of the article.)

accompanied by the secondary phase  $\text{La}_2\text{O}_3$  (PDF 01-074-2430 and 03-065-3185). Iron or manganese oxide phases could not be identified. YFPO and YMPO show hexagonal  $\text{YFeO}_3$  (PDF 00-048-0529) and  $\text{YMnO}_3$  (PDF 00-025-1079) structure with  $\text{Y}_2\text{O}_3$  (PDF 00-044-0399) as a secondary phase. Reflections of minor phases, e.g.  $\text{Fe}_2\text{O}_3$  and  $\text{Mn}_2\text{O}_3$  overlap with those of the perovskite phases, thus making any assignment or Rietveld refinement difficult. Pd addition does not produce changes of the lattice parameters of the host perovskite-type oxide and no reflection of Pd or  $\text{PdO}$  are observed, thus suggesting the high palladium dispersion.

Calcination further improves the phase purity and the crystallinity (Fig. 1). All catalysts maintain their original crystal structure except LMPO, which undergoes transition to the rhombohedral  $\text{La}_{0.93}\text{MnO}_3$ -type structure (PDF 01-082-1152). The crystallite size does not vary noticeably upon calcination at 700 °C. On the contrary, the phase purity is largely improved (94–97 wt%) despite the remaining  $\text{La}_2\text{O}_3$  and  $\text{Y}_2\text{O}_3$  secondary phases. It is noteworthy that  $\text{Y}_2\text{O}_3$  is formed in the metastable monoclinic phase, which is stable against heat treatment at 700 °C. This phase is not observed in the conventional wet synthesis method [16] and is likely the result of the short residence time at high temperature in the flame [39].

The morphology of the fresh and calcined catalysts and the state of palladium are addressed by HR-(S)TEM. Under the applied conditions of FSS, the droplet-to-particle formation mechanism

dominates but includes a disruption of droplets due to the additional combustible fuel in the water [23,40]. Thus, the flame-made catalysts exhibit bimodal particle size distribution [22], namely homogeneous nano-particles of around 20 nm together with spherical particles of 0.5–1  $\mu\text{m}$  in diameter (Fig. S4).

The relatively high vapour pressure of noble metals compared to perovskite-type oxides allows the deposition of Pd nano-particles on the support [20]. Small Pd particles of 2–5 nm with metallic and oxidic character are visible on LFPO (Fig. 2a and Fig. S5) [36]. The calcined catalysts show similar morphology (Fig. 2b) but display some particle aggregation. The average particle size is still around 20 nm, which is lower than the value obtained from the Scherrer equation. This is caused by the contribution of larger particles to the XRD estimation. The fresh and calcined LMPO, YFPO and YMPO (Fig. 2) show similar particle size and morphology to LFPO. The better Z-contrast offered by the lighter Y enables the observation of 2–5 nm Pd nano-particles in the STEM mode (Fig. 3). On a qualitative base, calcination at 700 °C appears to decrease the Pd dispersion on both YFPO and YMPO. Nevertheless, HR-TEM and STEM reveal that the fresh catalysts contain well-defined and dispersed Pd nano-particles rather than a solid solution between the perovskite-type oxide and Pd. However, it cannot be excluded that a fraction of palladium is incorporated in the perovskite crystal structure.

The reduction characteristics of the calcined catalysts are studied by  $\text{H}_2$ -TPR and the corresponding reduction profiles are presented in Fig. 4. The reduction of Pd-free catalysts is characterized by a series of events over the whole temperature range that are associated with the stepwise reduction of  $\text{Fe}^{4+}$  or  $\text{Mn}^{4+}$  species, which originate either from amorphous phases or from secondary species not observable by XRD [41,42]. Such species accompany the  $\text{La}_2\text{O}_3$  and  $\text{Y}_2\text{O}_3$  for stoichiometry balance. High temperature peaks originate from reduction of bulk species [42,43], whereas  $\text{YFeO}_3$  reduces to  $\text{Y}_2\text{O}_3$  and  $\text{Fe}^0$  [44].

Addition of Pd changes substantially the appearance of the  $\text{H}_2$ -TPR profiles (Fig. 4). The reduction features of B-site cations are shifted to lower temperature compared to the profiles of Pd-free perovskite-type oxides, likely due to hydrogen spillover. The perovskite-type oxide can stabilize Pd against reduction up to ca. 300 °C as a result of the formation of the solid solution [31], while Pd exposed on the surface is responsible for the low temperature reduction. This is observed in LFPO and YFPO where a sharp and intense peak appears below 80 °C, which is readily assigned to the reduction of  $\text{Pd}^{2+}$  to  $\text{Pd}^0$ . LFPO and YFPO prepared by FSS behave clearly differently compared to similar catalyst compositions prepared by the conventional citric acid method [16]. In contrast, LMPO and YMPO display a large  $\text{H}_2$  consumption at ca. 145 °C, which is likely a combination of the reduction of  $\text{Pd}^{2+}$  and  $\text{Mn}^{4+}$  [16] and mirrors the reduction characteristics obtained from the sample prepared by the citric acid method. The two synthesis methods thus provide structurally similar Mn-containing samples. The presence of the low temperature reduction events (<200 °C) in the calcined catalysts confirms that a considerable fraction of Pd is exposed on the perovskite surface.

The oxygen storage capacity complete (OSCC) determined as the total amount of oxygen desorbed from the catalysts at 400 °C is given in Table 1. OSCC is composition and surface area dependent and correlates well with the  $\text{H}_2$  uptake shown in Fig. 4. Y- and Mn-based catalysts exhibit higher OSCC values compared to La- and Fe-based ones. The values for the FSS catalysts are comparable to those reported for similar catalyst compositions [45,46]. Except for LFO, the presence of Pd improves OSCC due to a more facile hydrogen dissociation and increase of the oxygen mobility. The OSCC values determined for the perovskite-type catalysts are much larger than that of the Pd/ACZ reference sample (150  $\mu\text{mol O}_2/\text{g}$ ) reflecting their high reactivity.

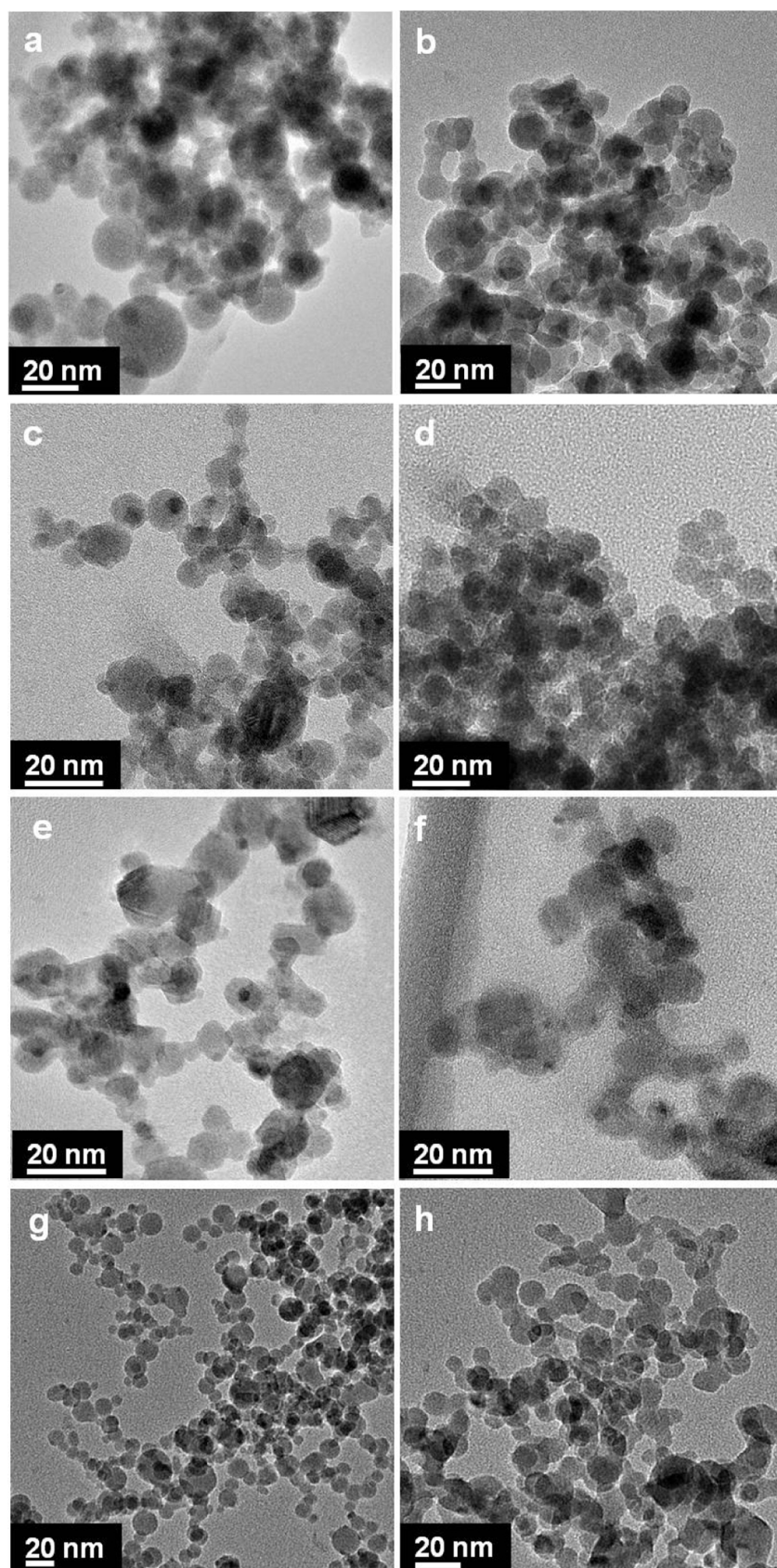


**Fig. 2.** HR-TEM of fresh (left) and calcined (right) LFPO (a and b), LMPO (c and d), YFPO (e and f), and YMPO (g and h).

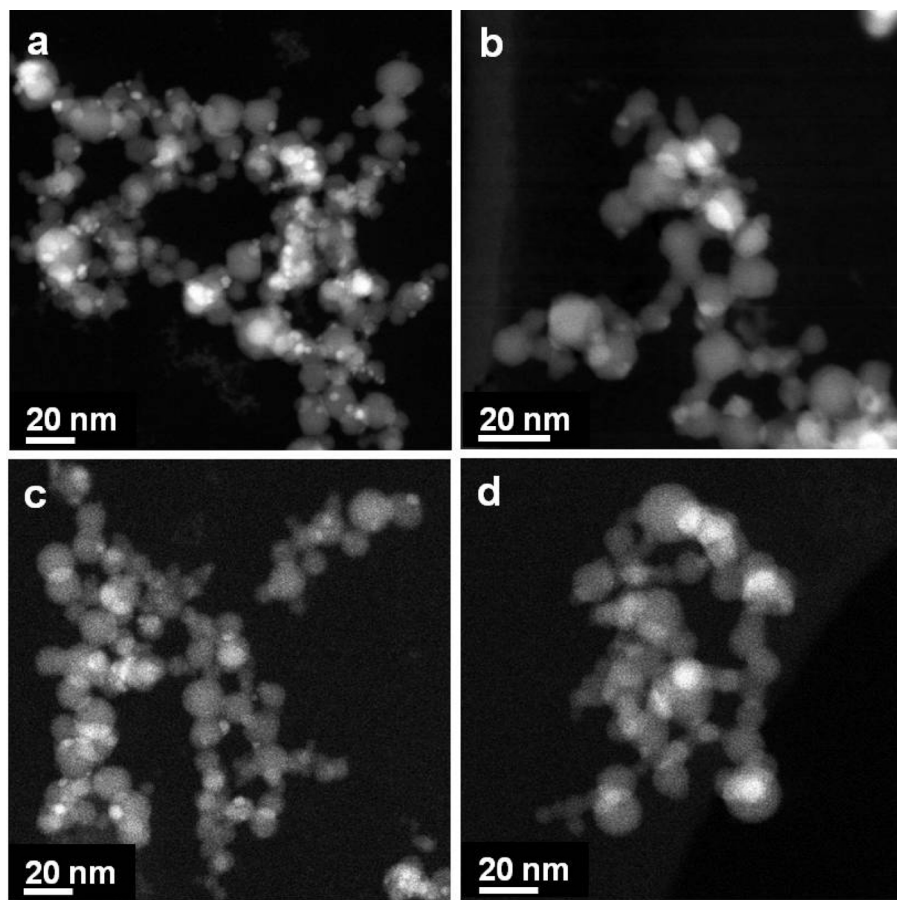


**Fig. 3.** HAADF-STEM of (a) fresh and (b) calcined YFPO, (c) fresh and (d) calcined YMPO.

Infrared spectroscopy of probe molecules is commonly used to obtain structural information of supported noble metal catalysts. This technique provides qualitative representation of the metal dispersion that can be complementary to the TEM observations, especially for samples with insufficient Z-contrast for HR-(S)TEM. The DRIFT spectra obtained during CO adsorption after in situ pretreatment in air at 500 °C followed by reduction in hydrogen at 300 °C display signals below 1650 cm<sup>-1</sup> corresponding to various carbonate species (Fig. S6). We consider that CO uptake by the support and reduction of the support itself are the main reasons for the failure of obtaining reasonable values for Pd dispersion by H<sub>2</sub> or CO chemisorption. Coordination of CO to Pd in the various catalysts (Fig. 5) provide three signals in the carbonyl region, i.e. at 2100 cm<sup>-1</sup> (linearly bonded CO), at 1984 cm<sup>-1</sup> ( $\mu_2$ -bridge bonded CO on Pd(100) facets and edges) and in the range of 1930–1750 cm<sup>-1</sup> (broad band resulting from  $\mu_3$ -hollow/multiple bonded CO on Pd(111) planes) which can be assigned according to the available literature [47–49]. The major difference between the DRIFT spectra of the catalysts is represented by intensity

variations. The relatively narrow and symmetric band of linearly adsorbed CO suggests the well-defined adsorption geometry. The high intensity ratio of the signal of linearly adsorbed CO to that of bridge-bonded CO ( $A_{2100}/A_{1984}$ ) reflects a greater contribution of adsorption on particle edges and corners than on terrace sites [48]. Because the fraction of terrace Pd atoms decreases with decreasing particle size [50], the average Pd particle size can be considered decreasing (alternately, the  $A_{2100}/A_{1984}$  ratio increasing) in the order YMPO > YFPO > LMPO ~ LFPO. The general signal attenuation upon calcination at 700 °C suggests less adsorption sites for CO, thus larger Pd particles. However, this phenomenon cannot be simply interpreted by the sintering of Pd particles, because where the linear CO signal is visible the  $A_{2100}/A_{1984}$  ratio remains largely unchanged thus reflecting the good dispersion of Pd particles. The intensity of the signals obtained on YFPO (note the scale bar in Fig. 5) indicates that the catalyst retains the highest Pd dispersion among the calcined catalysts. YMPO and LMPO show very weak linear and bridged bound CO signals, which suggest sintering of Pd particles.

**Table 2**

Atomic ratios (%) of surface cations for fresh and calcined Pd-containing catalyst obtained from XPS.

		La 3d5	Fe 2p	Mn 2p	Y 3d	Pd 3d	O 1s	C 1s	Pd/A	A/B
LFPO	Fresh	9.8	13.8	0	0	1.7	53	21.8	0.173	0.71
	Calc.	9.5	24.8	0	0	1.2	46.4	18.1	0.126	0.38
YFPO	Fresh	0	13.2	0	13.6	1.1	52.8	19.3	0.081	1.03
	Calc.	0	18.7	0	14.1	1.2	48.8	17.3	0.085	0.75
LMPO	Fresh	12.4	0	13.7	0	1.2	55.0	17.6	0.097	0.91
	Calc.	9.3	0	17.5	0	1.4	50.6	21.2	0.151	0.53
YMPO	Fresh	0	0	20.4	10.8	1.3	49.9	17.6	0.120	0.53
	Calc.	0	0	22.3	9.6	1.2	49.2	17.6	0.125	0.43

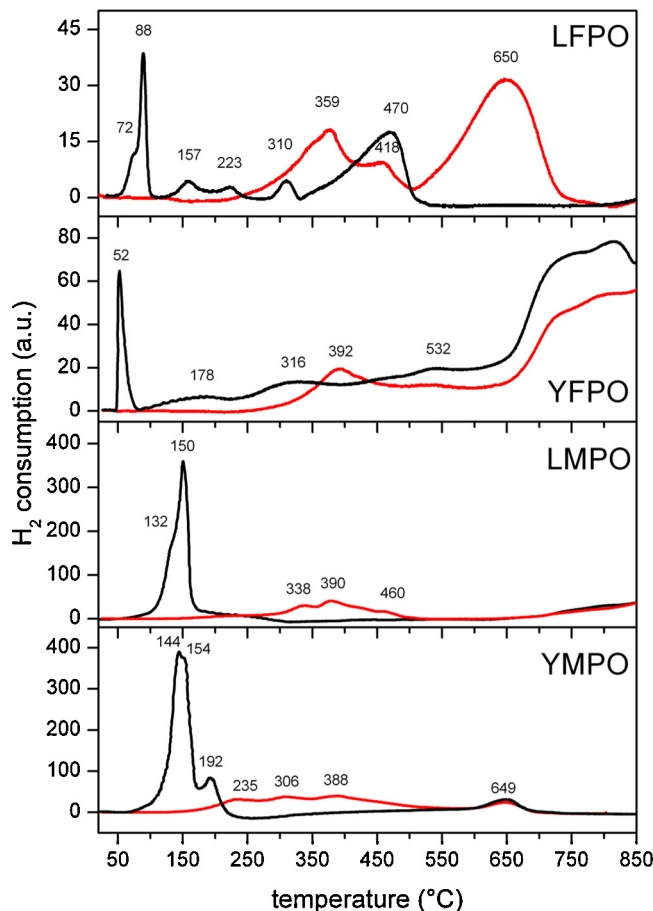


**Fig. 4.**  $\text{H}_2$ -TPR profiles of calcined Pd-free (red) and Pd-containing (black) catalysts. (For interpretation of the references to color in figure legend, the reader is referred to the web version of the article.)

### 3.2. The valence state of palladium

The surface composition and the Pd oxidation state are analyzed by X-ray photoelectron spectroscopy (XPS). The relative surface cationic composition in calcined catalysts is obtained from survey scans (Table 2). The Pd content in all catalysts is higher than the nominal stoichiometry (0.7 at% for Y-based catalysts and 0.9 at% for La-based catalysts) suggesting a Pd-enriched surface in agreement with the formation of Pd nano-particles as observed by TEM and DRIFTS. The large variation of ratio between surface concentrations of A and B site cations (A/B) indicates a heterogeneous surface composition of the samples, which reflects the presence of other phases than the main  $\text{ABO}_3$  perovskite-type phase.

The photoelectron spectra of the Pd 3d core level are presented in Fig. 6. In general, the binding energy (BE) of the Pd 3d<sub>5/2</sub> level varies depending on the nature of the Pd species, i.e. 335–335.4 eV for metallic Pd, 336.3–336.6 eV for  $\text{Pd}^{\text{II}}\text{O}$  and 337.9–338.2 eV for  $\text{Pd}^{\text{IV}}\text{O}_2$  [51–53]. The spectra of all fresh catalysts in Fig. 6 show a clear feature at ca. 335.5 eV that unambiguously confirms the presence of metallic Pd. The signal is systematically accompanied by a second one at roughly constant position irrespective of material composition (337.2 eV), which is attributed to  $\text{Pd}^{n+}$  species or  $\text{Pd}^{2+}$  species in unusual coordination environment [34,57]. Clearly, the spectrum of LFPO does not conform to the one obtained for the same catalyst composition prepared by the citric acid method ( $\text{LaFe}_{0.95}\text{Pd}_{0.05}\text{O}_{3\pm\delta}$ ) [31] and containing Pd predominantly in octahedral coordination within the  $\text{LaFeO}_{3\pm\delta}$  lattice (BE = 337.7 eV). Additionally, the surface Pd concentration

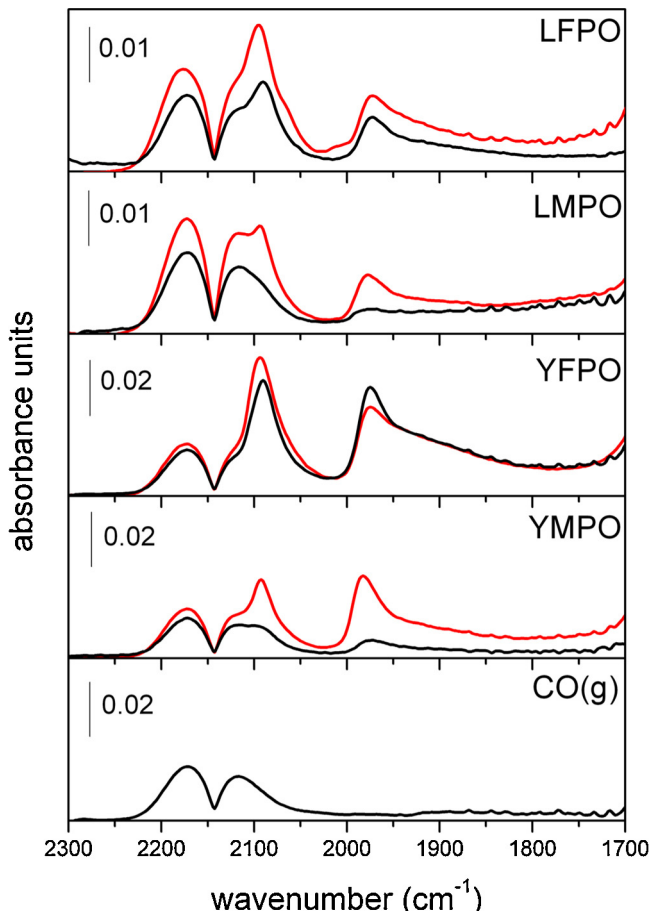


**Fig. 5.** DRIFT spectra of adsorbed CO on fresh (red) and calcined (black) catalysts after reduction at 300°C. (For interpretation of the references to color in figure legend, the reader is referred to the web version of the article.)

of the fresh LFPO synthesized by FSS is the highest among the catalysts produced by this method. These observations indicate that the catalyst structure obtained from FSS is different from that obtained by the conventional wet chemical method and the deposition of Pd nano-particles is achieved.

After calcination at 700°C, the photoelectron spectra exhibit relatively well-defined sharp signal of palladium oxide ( $\text{Pd}^{2+}$ ). The position of the signal varies between 336.5 and 336.9 eV in Fe and Mn containing samples, respectively. The signal of LFPO and YFPO still demonstrates some asymmetry on the high energy side that is indicative of a fraction of  $\text{Pd}^{n+}$  species ( $n > 2$ ). This observation is confirmed by the values of the full width at half maximum that is 2.14 and 2.34 eV for LFPO and YFPO, respectively compared to 1.41 and 1.56 eV for LMPO and YMPO, respectively. Therefore, the result of calcination is the formation of predominantly  $\text{Pd}^{2+}$  species that in the Fe-containing samples are accompanied by a persistent minority of  $\text{Pd}^{n+}$  species ( $n > 2$ ).

Major differences between the XPS of the catalysts lie in the intensity variations, like in the DRIFTS data. In terms of relative intensity ratio of the XPS signals ( $I_{337}/I_{335}$ ), fresh LFPO and YFPO demonstrate the least and most contribution from metallic Pd, respectively. The fresh LMPO and YMPO display very similar  $I_{337}/I_{335}$  ratio and higher contribution of metallic Pd compared to LFPO. Furthermore, the surface Pd concentration with respect to the A-site cation increases upon calcination at 700°C (Table 2), except for LFPO for which the Pd/La ratio decreased. On the other hand, the surface A/B ratio decreases in all catalysts, most likely as a result of the increased phase purity of the perovskite-type oxide

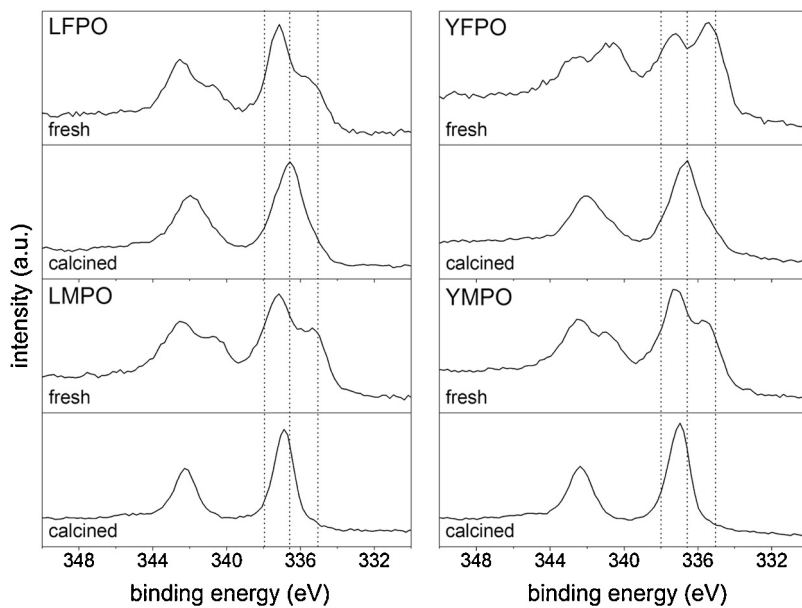


**Fig. 6.** X-ray photoelectron Pd 3d core level spectra of fresh and calcined catalysts. Vertical lines indicate photon electron peak positions of Pd<sup>0</sup>, Pd<sup>2+</sup> and Pd<sup>4+</sup>, from the right to the left, as reported in the text.

at the expenses of single oxide phases. Assuming that the phase purity improvement upon calcination observed by XRD and therefore the A/B ratio do not influence the Pd/A ratio significantly, the data in Table 2 reveal that the increase of surface Pd concentration for LMPO, YFPO and YMPO upon calcination is caused by the increase of the fraction of Pd being stabilized in form of particles. The anomalous decrease of the surface Pd concentration on LFPO may be the result of the strong interaction between LFO and Pd that keeps a fraction of Pd within the perovskite lattice making it elusive for XPS detection (penetration depth of 5–10 nm) [31].

The oxidation state and coordination environment of Pd are further characterized by X-ray absorption spectroscopy. The spectra of the various samples at the Pd K-edge are shown together with the reference Pd metal foil and PdO in Fig. 7 (the corresponding  $k^3$ -weighted  $\chi(\kappa)$  is shown in Fig. S7). The spectrum of the reference Pd/ACZ sample is also shown as an example of supported

PdO catalyst. The features of metallic Pd clearly contribute to the white line of the spectra of the fresh samples thus confirming the partially reduced state of Pd (Fig. 7a). This is supported by the non-phase shift corrected  $k^3$ -weighted Fourier transformed EXAFS spectra (Fig. 7c) exhibiting a clear contribution from the Pd–Pd shell at 2.5 Å. A major contribution to the FT spectra is also given by a first Pd–O shell at 1.6 Å attributed to the fraction of Pd in higher oxidation state. The missing second Pd–O–Pd coordination shell at ca. 3 Å supports the very fine dispersion of Pd–O species in the fresh FSS samples [19]. No obvious information on octahedrally coordinated Pd is obtained from the XANES data. This species is characterized by a typical doublet around the white line that is the fingerprint of its coordination environment [31]. Specifically for LFPO, this species corresponds to the one that is labelled as Pd<sup>n+</sup> in the above XPS spectra that characterizes the strong interaction between LFO and Pd. With this in mind, the spectrum of LFPO appears to be different

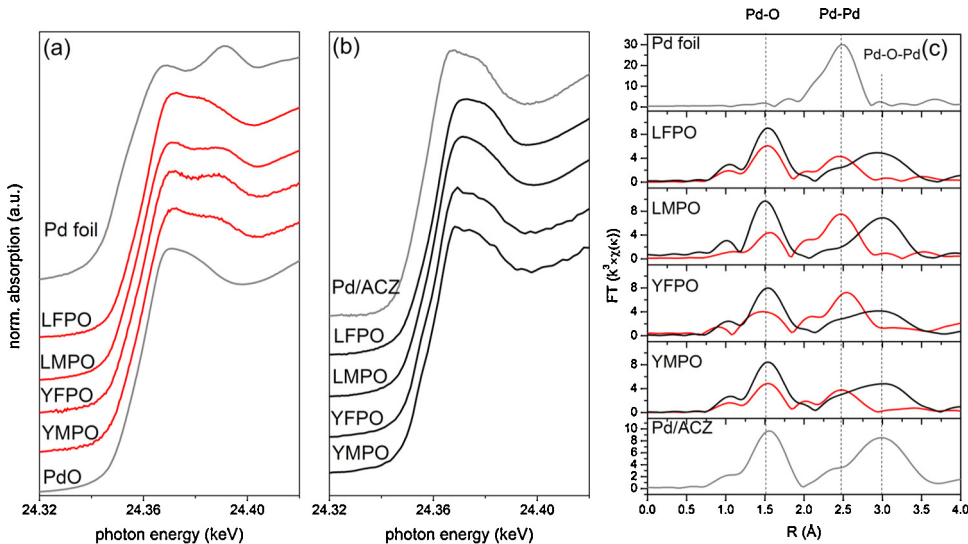


**Fig. 7.** Normalized XANES spectra at the Pd K-edge of (a) fresh and (b) calcined catalysts. Reference spectra of PdO and Pd metal foil are also provided for comparison together with the spectrum of Pd/ACZ. (c) Corresponding non-phase shifted  $k^3$ -weighted Pd K-edge FT spectra of fresh (red) and calcined catalysts (black). (For interpretation of the references to color in figure legend, the reader is referred to the web version of the article.)

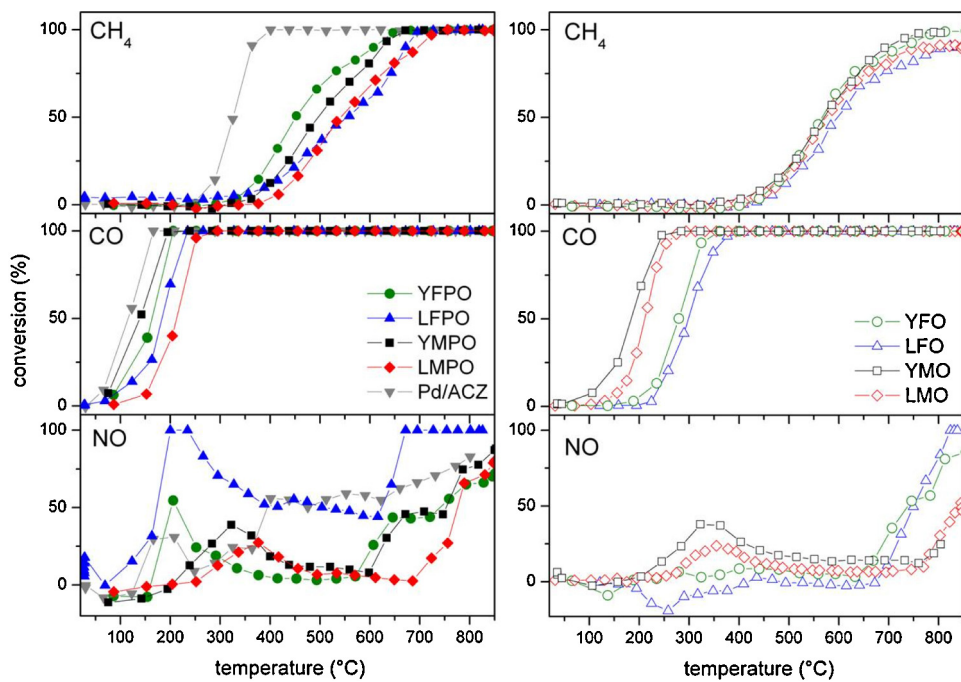


Fig. 8. CH<sub>4</sub>, CO and NO conversion profiles of calcined Pd-containing catalysts and Pd/ACZ (left panel), Pd-free catalysts (right panel).

from those of the other catalysts and shows less contribution from metallic Pd in agreement with the XPS data. The linear combination analysis considering metallic Pd, bulk PdO and Pd in octahedral coordination as in LaFe<sub>0.95</sub>Pd<sub>0.05</sub>O<sub>3</sub> [31] as possible contributions provides an estimate of the relative content of each species. Comparison between fresh and calcined LFPO reveals that the metallic Pd (17%) present in the fresh catalyst vanished upon calcination, whereas the fractions of Pd<sup>2+</sup> species increased (from 38 to 60%). No significant variation is observed for Pd<sup>n+</sup> species ( $n > 2$ ). The estimation is in line with the XPS data suggesting the presence of two species after calcination at 700 °C and indicating the loss of surface Pd concentration (Table 2). This is in agreement with the propensity of LFO to accommodate Pd within the lattice. The same procedure for LMPO reveals a higher content of metallic Pd in the fresh sample, again in agreement with the XPS data and indicates that after calcination 86% and 14% of Pd was in the 2+ and n+ ( $n > 2$ ) oxidation states, respectively. This confirms the general difficulty that we have faced to introduce Pd into LaMnO<sub>3±δ</sub>, which is in strong contrast to LaFeO<sub>3±δ</sub> [16]. For the Y-containing formulations, the linear combination analysis is not meaningful because of the different coordination environment that Pd can adopt at the B-site of YFeO<sub>3±δ</sub> and YMnO<sub>3±δ</sub> [15,54].

The XANES spectra confirm the observation obtained from XPS that no detectable metallic Pd is present after calcination (Fig. 7b). The white lines are very close to that of a typical supported PdO catalyst (e.g. Pd/ACZ). The contribution from the first Pd-Pd shell of metallic Pd also vanishes in the corresponding FT-EXAFS spectra, whereas a clear contribution at ca. 3 Å (Pd—O—Pd) and the increase of that at 1.6 Å indicate the formation of a well-defined PdO phase. Therefore, after calcination Pd is present predominantly in the form of supported PdO particles.

### 3.3. Three-way catalytic activity

The CH<sub>4</sub> and CO oxidation and NO reduction activities of the calcined catalysts are determined in a simulated exhaust feed comprising CO, CH<sub>4</sub>, NO and O<sub>2</sub> ( $\lambda = 1$ ) between 25 °C and 850 °C

(Fig. 8). The Pd-free catalysts demonstrate comparable CH<sub>4</sub> and CO oxidation activity between 400 °C and 800 °C. In contrast to the Y-containing samples, LFO and LMO do not show complete conversion even at 800 °C. In this temperature regime, methane oxidation is typically influenced by oxygen mobility of the bulk material. Addition of Pd produces substantial activity differences and lowers the temperature required for 50% methane conversion ( $T_{50}^{\text{CH}_4}$ ). The order of activity of the catalysts in terms of  $T_{50}^{\text{CH}_4}$  is: YFPO (450 °C) < YMPO (497 °C) < LMPO (542 °C) < LFPO (557 °C). Therefore, YFPO is the most active catalyst. However, it is also evident that YFPO is still less active than the reference Pd/ACZ catalyst.

The CO oxidation activity window of the flame-made catalysts (Fig. 8) is much narrower and closer to the activity of the reference catalyst than it is for CH<sub>4</sub> oxidation. The Pd-free catalysts demonstrate the typical interesting CO oxidation activity [55]. However, the difference among the catalysts is more evident than in the case of methane oxidation and the activity order ( $T_{50}^{\text{CO}}$ ) is YMO < LMO < YFO < LFO. This indicates that the nature of the perovskite-type oxide strongly influences its ability to exchange surface oxygen and thus their activity for CO oxidation, which is supported by the OSCC values of the Pd-free samples (YMO > LMO > YFO > LFO, and Table 1). The CO oxidation activity improves significantly in the presence of Pd as revealed by the shift of the light-off curves to lower temperature by ca. 100–150 °C. Activity differences between the catalysts are attenuated indicating that exposed Pd on the catalyst surface primarily dictates CO oxidation activity, however without excluding the role of the perovskite-type oxide. The differentiation of activity for methane oxidation upon addition of Pd is obviously also attributed to the presence of the precious metal. The methane oxidation efficiency of the catalysts strongly depends on the nature of the interaction between Pd and the perovskite-type oxide and on the nature of the Pd species present in the catalysts [16,31]. This latter parameter strongly depends on the nature of the perovskite-type oxide [16]. The various Pd species that are detected on the catalysts differently affect the activity for methane oxidation. Supported PdO nano-particles are certainly the active species [31,56] compared to the Pd<sup>n+</sup> ( $n > 2$ ) species observed in different levels in the samples.

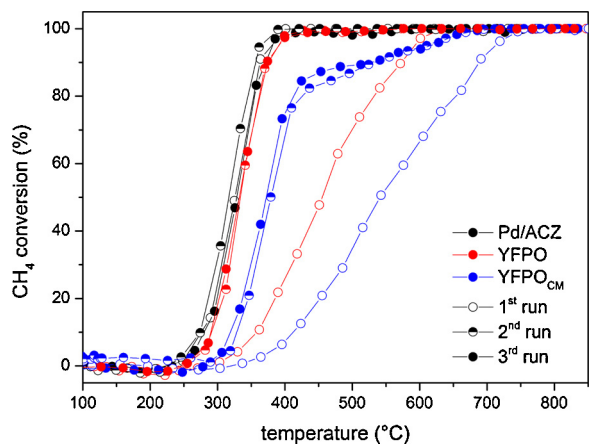


Fig. 9.  $\text{CH}_4$  conversion profiles for three consecutive reaction runs on Pd/ACZ, YFPO and YFPO<sub>CM</sub>.

The Pd-free catalysts exhibit NO reduction activity above 600 °C with the exception of the Mn-containing catalysts LMO and YMPO that also display NO conversion below 400 °C. Upon addition of Pd, low temperature activity develops. In the case of Fe-based catalysts, the first NO conversion event is correlated with CO oxidation activity and is therefore associated with NO reduction by CO. On the contrary, Mn-based catalysts display NO reduction activity between 300 and 400 °C, therefore at the end of CO oxidation. The NO conversion event observed above 600 °C does not coincide with the onset of methane oxidation. It rather appears at full methane conversion and can thus hardly be associated with NO reduction by methane. Based on the GC data at hand we cannot precisely assess the origin of the complex NO reduction activities demonstrated by the catalysts. However, it should be noted that LFPO demonstrates remarkable low temperature NO reduction activity with full conversion at 200 °C and a relatively wide activity window above 50% conversion (ca. 160–390 °C) that is in agreement with previous reports [45,57].

#### 3.4. Activation

Consecutive runs of catalytic activity under stoichiometric conditions are carried out in the 100–850 °C temperature range in order to explore catalyst stability after exposure to high temperature during reaction. The corresponding light-off curves for  $\text{CH}_4$  oxidation in the heating segment are shown in Fig. 9 for Pd/ACZ and YFPO. Pd/ACZ does not show significant alteration of activity over three consecutive runs. In marked contrast, the perovskite-type oxide YFPO exhibits a large improvement of  $\text{CH}_4$  oxidation activity in the second reaction run that is maintained in the third one. The  $T_{50}^{\text{CH}_4}$  (450 °C) is lowered to ca. 330 °C providing an improvement by 120 °C. All perovskite-type samples display such activation behaviour and the corresponding values of  $T_{50}^{\text{CH}_4}$  in the consecutive reaction cycles are reported in Table 3. LFPO and LMPO display the largest activity improvement in the series ( $\Delta T_{50}^{\text{CH}_4} = 166$  °C). However, LFPO remains the catalyst with the highest  $T_{50}^{\text{CH}_4}$ ; the  $T_{50}^{\text{CH}_4}$  order in the third reaction run is YFPO < YMPO < LMPO < LFPO. No activity improvement is observed for CO oxidation. On the contrary, NO reduction activity is largely improved (not shown in Fig. 9 for simplicity) and already in the second run YFPO exhibits identical activity to that of Pd/ACZ.

Given its performance, YFPO is further selected for a comparison with the same catalyst composition prepared in a single step by the conventional citric acid method and calcined at 700 °C (YFPO<sub>CM</sub>, Fig. 9). The two samples exhibit identical OSCC (Table 1). In the first

activity run, the conversion profiles for the three pollutants of the FSS catalyst are generally shifted to lower temperature despite the lower Pd content (Table 1). In particular,  $T_{50}^{\text{CH}_4}$  is ca. 90 °C lower than that of YFPO<sub>CM</sub> (Fig. 9). Despite the analogous activation and the even larger  $\Delta T_{50}^{\text{CH}_4}$  (173 °C) of YFPO<sub>CM</sub> on repeated reaction runs, the flame-made catalyst demonstrates the most active in terms of  $T_{50}$ , revealing that the structure obtained from FSS is more favourable than that obtained by the conventional citric acid method in a single step.

A preliminary characterization of Pd/ACZ, YFPO and YFPO<sub>CM</sub> is carried out after the three repeated reaction runs of Fig. 9 using STEM(-EDX) and XRD. STEM of Pd/ACZ (Fig. 10a) testifies only an increase of the average Pd particle size from 8 to ca. 11 nm compared to the fresh catalyst (not shown). Due to the short exposure to high temperature during reaction, the YFO support particles display some degree of coalescence (Fig. 10b), whereas the size of Pd particles increases significantly and well-defined and shaped particles of ca. 25 nm become visible (inset of Fig. 10b). The small particle size of the support does not allow the determination of a possible distribution of particle sizes. The large YFO particles of Fig. 10b likely reflect the phase transformation from hexagonal to orthorhombic YFO experienced by the catalyst that is observed after the three reaction runs by XRD (Fig. 11). We argue that Pd can stabilize the hexagonal phase [15] when it is able to strongly interact with the mixed metal oxide, i.e. it adopts the same coordination environment of the B-site cation. In contrast, the presence of well-defined Pd nano-particles as in the flame-made catalyst does not seem to be able to prevent the phase transition to the orthorhombic phase. The presence of a metallic Pd phase (PDF 01-088-2335) is confirmed by the Pd(1 1 1) reflection at  $2\theta$  ca. 40°. Particle growth of the active metal component is also observed in the case of YFPO<sub>CM</sub> (Fig. 10d). A clear bimodal particle size distribution is observed after the third reaction run with well dispersed particles (ca. 6.7 nm) coexisting with larger particles (ca. 27 nm), in strong contrast to the situation of the fresh state (Fig. 10c). Therefore, Pd particle size and distribution change and extensive reduction takes place upon the repeated reaction runs.

The catalytic activity data indicates that YFO and Y-based catalysts are a suitable perovskite-type composition for methane oxidation in general [16]. It is likely that the high Pd dispersion and deposition of PdO on the YFO support are mainly responsible for the observed interesting TWC properties. In the flame-made catalyst and under these synthesis conditions, Pd does not adopt the coordination environment that is expected from the hexagonal structure of  $\text{YFeO}_{3\pm\delta}$  and displays a similar coordination to that of stabilized PdO on metal oxide supports. This may not exclude some degree of interaction between YFO and Pd [15]. However, this is in agreement with our previous observation that Pd clearly segregates in form of  $\text{Pd}^{2+}$  (PdO) species at the  $\text{YFeO}_{3\pm\delta}$  surface depending on the calcination temperature and after experiencing high temperature (850–900 °C) during methane oxidation under lean conditions

Table 3  
 $T_{50}$  for  $\text{CH}_4$  conversion of three consecutive reaction runs under stoichiometric conditions.

Entry name	$T_{50}^{\text{CH}_4}$ (°C)			
		1st run	2nd run	3rd run
LFPO	557	394	391	
LMPO	542	361	376	
YFPO	450	333	332	
YMPO	497	350	338	
YFPO <sub>CM</sub> <sup>a</sup>	543	381	370	
Pd/ACZ	326	316	328	

<sup>a</sup> Prepared by the amorphous citric acid method.

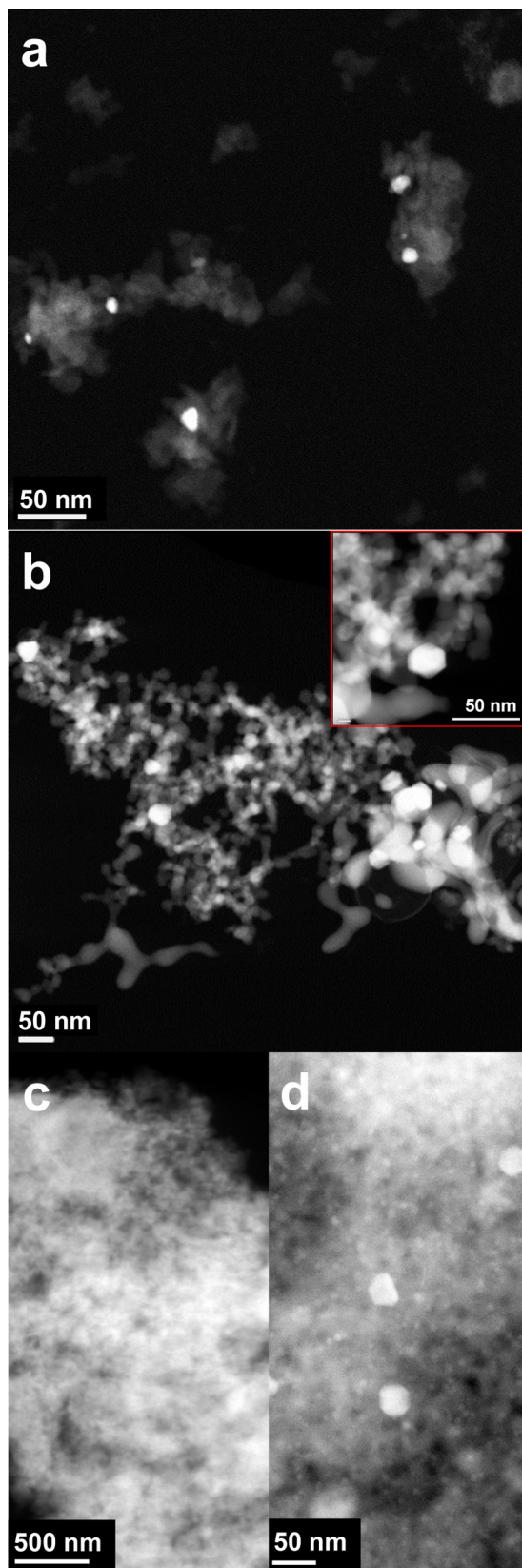


**Fig. 10.** STEM images of (a) Pd/ACZ, (b) YFPO and (d) YFPO<sub>CM</sub> after three consecutive reaction runs under stoichiometric conditions. (c) STEM image of calcined YFPO<sub>CM</sub> before reaction.

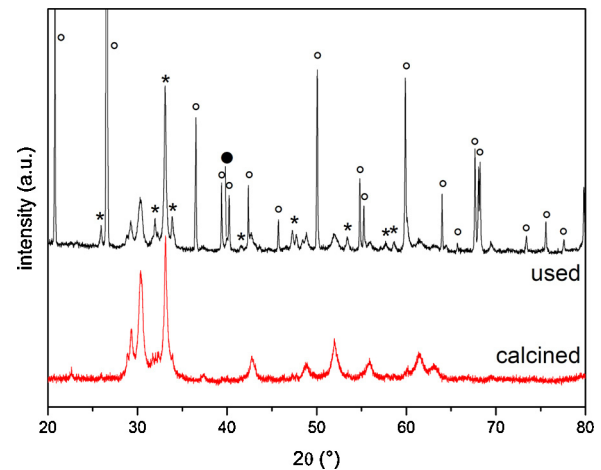


**Fig. 11.** XRD of calcined and used YFPO. The used sample refers to three consecutive activity runs under stoichiometric conditions. Symbols: (●) Pd, (\*) orthorhombic YFeO<sub>3</sub> and (○) sea sand.

[16]. Although the perovskite-type material may be involved during reaction because of its oxygen exchange properties, based on the observed activity improvement and of the above STEM images it is difficult to imagine that a process such as the self-regeneration observed on LFPO-type catalysts is extensively at work in this flame-made catalyst. On the other hand, the observation of the formation of metallic Pd particles after the three reaction runs of Fig. 9 does not necessarily imply that metallic Pd is the active species for methane oxidation under stoichiometric reaction conditions. Rather, bulk metallic Pd is the most realistic state of the active phase during reaction. The oxidation state of Pd in Pd/Al<sub>2</sub>O<sub>3</sub> and to a lesser extent in Pd/ACZ progressively changes from Pd<sup>2+</sup> to metallic Pd upon consecutive reaction cycles under stoichiometric conditions as a result of the exposure to high temperature and the thermodynamic equilibrium of the PdO–Pd pair [58,59]. The oscillating redox conditions used during operation can still provide the conditions for the formation of active surface PdO<sub>x</sub> species [60,61]. The formation of large metallic Pd particle and the coincident improvement of CH<sub>4</sub> oxidation activity well agree with a recent work demonstrating the enhanced activity of 20 nm diameter particles compared to ten times smaller nano-particles in Pd/Al<sub>2</sub>O<sub>3</sub> [62].

Although it may have similar Pd dispersion to YFPO, flame-made LFPO contains a fraction of incorporated Pd in the LaFeO<sub>3±δ</sub> lattice that is substantially inert to methane oxidation. Therefore, the difference of catalytic activity between the two catalysts can also be attributed to an effect that is similar to the Pd-loading one that is created by the strong interaction between the perovskite-type material and Pd at given metal loading [63]. Nevertheless, the fraction of Pd that is not directly available for reaction because interacting with the perovskite lattice may contribute to impart protective functions against ageing and promote oxygen mobility, characteristics that we are presently investigating. The effect of the presence of the Pd<sup>n+</sup> species ( $n > 2$ ) on catalytic activity should become observable when catalysis is evaluated under the typical oscillating redox conditions of TWC [7].

#### 4. Conclusions

Flame spray synthesis (FSS) is used to produce nano-scaled Pd-containing perovskite-type oxide catalysts potentially suitable for the abatement of methane under stoichiometric conditions. Nanocrystalline catalysts are obtained whose phase purity is improved after calcination at 700 °C. In contrast to the conventional citric acid

method, exposed Pd particles are deposited on the perovskite-type support, which seems crucial for the three-way catalytic activity. This is also the case for  $\text{LaFeO}_{3\pm\delta}$ . The Pd particles are a mixture of metallic Pd and a species assigned to Pd incorporated in the perovskite lattice. On the contrary,  $\text{PdO}$  is the dominant palladium species after calcination.

Among the investigated perovskite-type oxides,  $\text{YFeO}_{3\pm\delta}$  exhibits the best performance for methane oxidation under stoichiometric conditions in the presence of Pd, likely due to the high accessibility of Pd exposed at its surface. Therefore, this study confirms that the Y–Fe–O catalyst composition is an interesting one for methane oxidation in general. The improved performance of this catalyst compared to the same composition prepared by a conventional wet chemistry method is associated with the peculiar structure obtained by FSS. This peculiar structure is likely a combination of the dispersed  $\text{PdO}$  particles, the presence of a fraction of Pd in higher coordination state and the nano-size of the mixed Y–Fe–O oxide with improved oxygen exchange properties and surface area. Moreover, the YFPO catalyst experiences an activation process towards  $\text{CH}_4$  oxidation under stoichiometric reaction conditions that renders it as active as the reference TWC and therefore, an interesting material for further studies. The preliminary characterization of the catalyst after the repeated reaction cycles indicates that metallic Pd particles (ca. 20 nm) are present when activity improvement is observed. Therefore, this situation seems to favour the formation of a more active catalyst. Additionally, the catalyst experiences phase transformation and  $\text{YFeO}_3$  is partly converted into the orthorhombic phase.

The presence of well-defined Pd particles on the mixed oxide support, rather than Pd species dispersed within the perovskite-type lattice that is expected from the 'self-regenerative' catalysts based on the La–Fe–O composition, raises the question about the long-term stability of the catalysts under the typical redox TWC conditions. We are currently evaluating the ageing characteristics of Y–Fe–O based catalysts, where we should further demonstrate the potential of Pd in combination with  $\text{YFeO}_{3\pm\delta}$ .

## Acknowledgements

The authors kindly acknowledge the Swiss National Science Foundation (National Research Program SNF-NPF 62 Smart Materials, Project No. 406240-126127) for financial support. The authors would like to thank Dr. A. Pappacena (University of Udine, Italy) for the OSCC measurements. The staff of beamline X1 of Hasylab is acknowledged for support during beamtime. R. Figi is thanked for ICP-OES measurements and Ms. H. Widmer for her help in experimental work.

## Appendix A. Supplementary data

Supplementary data associated with this article can be found, in the online version, at <http://dx.doi.org/10.1016/j.apcatb.2013.08.001>.

## References

- [1] R.M. Heck, R.J. Farrauto, S.T. Gulati, *Catalytic Air Pollution Control: Commercial Technology*, 3rd ed., Wiley, Hoboken, New Jersey, 2009.
- [2] P. Gelin, M. Primet, *Applied Catalysis B* 39 (2002) 1.
- [3] A. Winkler, P. Dimopoulos, R. Hauert, C. Bach, M. Aguirre, *Applied Catalysis B* 84 (2008) 162.
- [4] Y. Nishihata, J. Mizuki, T. Akao, H. Tanaka, M. Uenishi, M. Kimura, T. Okamoto, N. Hamada, *Nature* 418 (2002) 164.
- [5] J.P. Dacquin, M. Cabie, C.R. Henry, C. Lancelot, C. Dujardin, S.R. Raouf, P. Granger, *Journal of Catalysis* 270 (2010) 299.
- [6] M.B. Katz, G.W. Graham, Y. Duan, H. Liu, C. Adamo, D.G. Schlom, X. Pan, *Journal of the American Chemical Society* 133 (2011) 18090.
- [7] A. Eysller, E. Kleymenov, A. Kupferschmid, M. Nachtegaal, M. Santhosh Kumar, P. Hug, A. Weidenkaff, D. Ferri, *The Journal of Physical Chemistry C* 115 (2011) 1231.
- [8] E. Tzimpilis, N. Moschoudis, M. Stoukides, P. Bekiaroglou, *Applied Catalysis B* 84 (2008) 607.
- [9] M.A. Pena, J.L.G. Fierro, *Chemical Reviews* 101 (2001) 1981.
- [10] D. Ferri, L. Forni, *Applied Catalysis B* 16 (1998) 119.
- [11] R. Shannon, *Acta Crystallographica A* 32 (1976) 751.
- [12] S. Mathur, M. Veith, R. Rapalaviciute, H. Shen, G.F. Goya, W.L. Martins Filho, T.S. Berquo, *Chemistry of Materials* 16 (2004) 1906.
- [13] X. Lü, J. Xie, H. Shu, J. Liu, C. Yin, J. Lin, *Materials Science and Engineering: B* 138 (2007) 289.
- [14] G. Pecchi, C. Campos, O. Pena, *Catalysis Today* 172 (2011) 111.
- [15] J. Li, U.G. Singh, T.D. Schlundt, J.K. Stalick, S.L. Scott, R. Seshadri, *Chemistry of Materials* 20 (2008) 6567.
- [16] A. Eysller, A. Winkler, O. Safonova, M. Nachtegaal, M. Santhosh Kumar, P. Hug, A. Weidenkaff, D. Ferri, *Chemistry of Materials* 24 (2012) 1864.
- [17] G.L. Chiarello, I. Rossetti, L. Forni, *Journal of Catalysis* 236 (2005) 251.
- [18] G.L. Chiarello, I. Rossetti, P. Lopinto, G. Migliavacca, L. Forni, *Catalysis Today* 117 (2006) 549.
- [19] G.L. Chiarello, J.-D. Grunwaldt, D. Ferri, F. Krumeich, C. Oliva, L. Forni, A. Baiker, *Journal of Catalysis* 252 (2007) 127.
- [20] R. Strobel, A. Baiker, S.E. Pratsinis, *Advanced Powder Technology* 17 (2006) 457.
- [21] A. Heel, A. Vital, P. Holtappels, T. Graule, *Journal of Electroceramics* 22 (2009) 40.
- [22] A. Heel, P. Holtappels, T. Graule, *Journal of Power Sources* 195 (2010) 6709.
- [23] A. Heel, P. Holtappels, P. Hug, T. Graule, *Fuel Cells* 10 (2010) 419.
- [24] B. Schimmoeller, S.E. Pratsinis, A. Baiker, *ChemCatChem* 3 (2011) 1234.
- [25] L. Maedler, H.K. Kammler, R. Mueller, S.E. Pratsinis, *Journal of Aerosol Science* 33 (2002) 369.
- [26] R. Strobel, S.E. Pratsinis, *Physical Chemistry Chemical Physics* 13 (2011) 9246.
- [27] E. Campagnoli, A. Tavares, L. Fabbri, I. Rossetti, Y.A. Dubitsky, A. Zaopo, L. Forni, *Applied Catalysis B* 55 (2005) 133.
- [28] R. Lanza, I. Rossetti, L. Fabbri, C. Oliva, L. Forni, *Applied Catalysis B: Environmental* 28 (2000) 55.
- [29] G.L. Chiarello, D. Ferri, J.D. Grunwaldt, L. Forni, A. Baiker, *Journal of Catalysis* 252 (2007) 137.
- [30] A. Vital, A. Angermann, R. Dittmann, T. Graule, J. Töpfer, *Acta Materialia* 55 (2007) 1955.
- [31] A. Eysller, P. Mandaliev, A. Winkler, P. Hug, O. Safonova, R. Figi, A. Weidenkaff, D. Ferri, *The Journal of Physical Chemistry C* 114 (2010) 4584.
- [32] E. Mamontov, R. Brezny, M. Koranne, T. Egami, *The Journal of Physical Chemistry B* 107 (2003) 13007.
- [33] J. Rodriguez-Carvajal, *Physica B: Condensed Matter* 192 (1993) 55.
- [34] P. Thompson, D.E. Cox, J.B. Hastings, *Journal of Applied Crystallography* 20 (1987) 79.
- [35] S.J. Pennycook, *Ultramicroscopy* 30 (1989) 58.
- [36] B. Van Devener, S.L. Anderson, T. Shimizu, H. Wang, J. Nabity, J. Engel, J. Yu, D. Wickham, S. Williams, *The Journal of Physical Chemistry C* 113 (2009) 20632.
- [37] B. Ravel, M. Newville, *Journal of Synchrotron Radiation* 12 (2005) 537.
- [38] P. Scherrer, *Göttinger Nachrichten Gesell 2* (1918) 98.
- [39] B. Guo, Z.-P. Luo, *Journal of the American Ceramic Society* 91 (2008) 1653.
- [40] L. Maedler, S.E. Pratsinis, *Journal of the American Ceramic Society* 85 (2002) 1713.
- [41] P. Ciambelli, S. Cimino, L. Lisi, M. Faticanti, G. Minelli, I. Pettiti, P. Porta, *Applied Catalysis B* 33 (2001) 193.
- [42] R. Zhang, H. Alamdar, S. Kaliaguine, *Journal of Catalysis* 242 (2006) 241.
- [43] B. Levasseur, S. Kaliaguine, *Journal of Solid State Chemistry* 181 (2008) 2953.
- [44] L. Carreiro, Y.T. Qian, R. Kershaw, K. Dwight, A. Wold, *Materials Research Bulletin* 20 (1985) 619.
- [45] M. Uenishi, H. Tanaka, M. Taniguchi, I. Tan, Y. Sakamoto, S. Matsunaga, K. Yokota, T. Kabayashi, *Applied Catalysis A* 296 (2005) 114.
- [46] J. Chen, M. Shen, X. Wang, J. Wang, Y. Su, Z. Zhao, *Catalysis Communications* 37 (2013) 105.
- [47] J.K.A. Clarke, G.M. Farren, H.E. Rubalcava, *The Journal of Physical Chemistry* 71 (1967) 2376.
- [48] T. Lear, R. Marshall, J.A. Lopez-Sanchez, S.D. Jackson, T.M. Klapötke, M. Bäumer, G. Rupprechter, H.J. Freund, D. Lennon, *Journal of Chemical Physics* 123 (2005) 1.
- [49] Y. Soma-Noto, W.M.H. Sachtler, *Journal of Catalysis* 32 (1974) 315.
- [50] R. van Hardeveld, F. Hartog, *Surface Science* 15 (1969) 189.
- [51] J.F. Moulder, J. Chastain, *Handbook of X-ray Photoelectron Spectroscopy: A Reference Book of Standard Spectra for Identification and Interpretation of XPS Data*, Physical Electronics, 1995.
- [52] K.S. Kim, A.F. Gossmann, N. Winograd, *Analytical Chemistry* 46 (1974) 197.
- [53] A.S. Marmede, G. Leclercq, E. Payen, P. Granger, L. Gengembre, J. Grimbolt, *Surface and Interface Analysis* 34 (2002) 105.
- [54] J.A. Kurzman, J. Li, T.D. Schlundt, C.R. Parra, X. Ouyang, R. Davis, J.T. Miller, S.L. Scott, R. Seshadri, *Chemistry of Materials* 50 (2011) 8073.
- [55] S. Royer, D. Duprez, *ChemCatChem* 3 (2011) 24.
- [56] M. Santhosh Kumar, M.H. Aguirre, A. Weidenkaff, D. Ferri, *The Journal of Physical Chemistry C* 114 (2010) 9443.
- [57] G.C. Mondragon Rodriguez, K. Kelm, S. Heiskens, W. Grunert, B. Saruhan, *Catalysis Today* 184 (2012) 184.
- [58] M. Santhosh Kumar, G.L. Chiarello, Y. Lu, A. Weidenkaff, D. Ferri, *Topics in Catalysis* 56 (2013) 239.

- [59] Y. Lu, M. Santhosh Kumar, G.L. Chiarello, P. Dimopoulos Eggenschwiler, C. Bach, M. Weilenmann, A. Spiteri, A. Weidenkaff, D. Ferri, *Catalysis Communications* 39 (2013) 55.
- [60] S. Cimino, M.P. Casaletto, L. Lisi, G. Russo, *Applied Catalysis A* 327 (2007) 238.
- [61] E. Tzimpilis, N. Moschoudis, M. Stoukides, P. Bekiaroglou, *Applied Catalysis B* 87 (2008) 9.
- [62] A. Yu, A.M. Batkin, N.S. Teleguina, G.O. Bragina, V.I. Zaikovsky, I.P. Prosvirin, A.K. Khudorozhkov, V.I. Bukhtiyarov, *Topics in Catalysis* 56 (2013) 306.
- [63] A. Eyssler, A. Winkler, P. Mandaliev, P. Hug, A. Weidenkaff, D. Ferri, *Applied Catalysis B* 106 (2011) 494.